Materials Research Bulletin 164 (2023) 112235

Contents lists available at ScienceDirect

Materials Research Bulletin

journal homepage: www.elsevier.com/locate/matresbu

Research Papers

First principles study on electronic and optical properties of Cu_2CoGeS_4 for photovoltaic conversion and photocatalytic applications

J. El hamdaoui [a,b], K. Lakaal [a,b], D. Mazkad [c], M. Beraich [d], A. El Fatimy [e], M. Courel [f], L.M. Pérez [g,**], Pablo Díaz [h], D. Laroze [i], E. Feddi [a,e,*]

[a] Group of Optoelectronic of Semiconductors and Nanomaterials, ENSAM, Mohammed V University in Rabat, Morocco
[b] Laboratory of Condensed Matter and Interdisciplinary Sciences (LaMCScI), Faculty of Sciences Rabat, Mohammed V University in Rabat, Morocco
[c] Laboratory of Spectroscopy, Molecular Modeling, Materials, Nanomaterials, Water and Environment, Materials for Environment Team, ENSAM, Mohammed V University in Rabat, Morocco
[d] Laboratory of Materials, Energy and the Environment (LaMEE), Faculty of Science Semlalia. Cadi Ayyad University, P. O. Box 2390, Marrakech 40000, Morocco
[e] Institute of Applied Physics, Mohammed VI Polytechnic University, Lot 660, Hay Moulay Rachid Ben Guerir, 43150, Morocco
[f] Universidad de Guadalajara, Centro Universitario de los Valles (CUValles), Ameca, Jalisco, México
[g] Departamento de Física, FACI, Universidad de Tarapacá, Casilla 7D, Arica, Chile
[h] Departamento de Ciencias Físicas, Universidad de La Frontera, Casilla 54-D, Temuco 4780000, Chile
[i] Instituto de Alta Investigación, CEDENNA, Universidad de Tarapacá, Casilla 7D, Arica, Chile

ARTICLE INFO

Keywords:
Kesterite
CCGS
Electronic properies
Optical properties
Solar cell

ABSTRACT

In this study, the structural, electrical, and optical characteristics of the Stannite Cu2CoGeS4 (CCGS) are investigated using first-principle calculations. Band gap energy is determined using both the mBJ + U and HSE potentials. Both methods yield to similar results (1.73 1.73 eV and 1.78 eV for the first and second, respectively and 1.78 eV for the first and second, respectively). Based on our numerical simulations, CCGS is a viable absorber material for solar systems due to its exceptionally high absorption coefficient (on the order of 10^4 cm^{-1}). This work also determines other optical parameters such as the refraction index and the dielectric function. In addition, the SCAPS program was used to conduct a simulation of solar cells based on CCGS. Based on the computed values of the short-circuit current density J_{sc}, open-circuit voltage V_{oc}, Fill factor FF, and power conversion efficiency, CCGS is presented as a good choice for solar cells. We also explored the potential of CCGS for photocatalytic water splitting.

1. Introduction

The growing energy demand and the need for sustainable energy sources have led to an increased interest in the development of solar cells as a potential solution. Thin film solar cells, in particular, have gained attention due to their potential for low-cost production and high efficiency [1]. However, the selection of suitable absorber materials in thin film solar cells is a challenging task, as several factors such as the absorption coefficient, band gap value, cost of production, stability, non-toxicity, and ease of fabrication must be considered [2].

Cu_2ZnSnS_4 (CZTS) quaternary compound has emerged as a promising absorber material in recent years due to its ease of fabrication and excellent properties [3]. This material has a p-type conductivity and absorption coefficient of more than 10^5 cm^{-1} with an optimal and direct band gap transition of 1.5 eV, allowing visible light absorption [4,5].

To address these limitations, new quaternary compounds Cu_2MNS_4 have attracted the attention of researchers. The general idea consists of the partial or total substitution of the Zn^{2+} by M^{2+} (M = Fe, Co, Ni, or Mn) and Sn^{4+} by $N^{4+} = Ge^{4+}$ [4,6–8]. These new quaternary materials crystallize in a tetragonal kesterite (I4 space group) or tetragonal stannite (I42m space group) system [6,8]. They have interesting properties similar to those of CZTS [9,10].

One of these new compounds is Cu_2CoGeS_4 (CCGS), a tetragonal stannite material. Despite its potential application, the improvement of its efficiency and the understanding of this type of cell remain relatively limited compared to CIGS and CdTe solar cells. CCGS has a direct transition with a wide optical range (1.4 eV to 2.2 eV) [11–13], making

* Corresponding author at: Group of Optoelectronic of Semiconductors and Nanomaterials, ENSAM, Mohammed V University in Rabat, Morocco.
** Corresponding author.
E-mail addresses: lperez@uta.cl (L.M. Pérez), e.Feddi@um5s.net.ma (E. Feddi).

https://doi.org/10.1016/j.materresbull.2023.112235
Received 9 December 2022; Received in revised form 25 February 2023; Accepted 14 March 2023
Available online 22 March 2023
0025-5408/© 2023 Elsevier Ltd. All rights reserved.

it suitable for using in various fields such as solar cells, photoelectrochemical cells, and photocatalytic applications.

Recent experimental studies have been focused on exploring the properties and potential applications of CCGS. Beraich et al. successfully synthesized and characterized thin films of Cu2CoGeS4 using the spray ultrasonic technique [11]. Meanwhile, Bernert et al. conducted the first theoretical and experimental examination of using CCGS for thermoelectric purposes [13]. Gulay et al. used density functional theory to analyze the lattice parameters, Mulliken population analysis, elastic constants, and thermal properties of stannite Cu2CoXS4 (X = Si, Ge, Sn) [12]. These studies offer valuable insights into the properties of CCGS for device applications. However, until now, there are neither reports concerning CCGS in solar cells nor its use as a photocatalytic material. In light of this, the present work aims to analyze the possible use of CCGS as an absorber material in solar cells and its photocatalytic application. An interesting approach to achieving this goal is to use numerical simulations. Therefore, in the present report, the density functional theory (DFT) calculation using WIEN2k and Quantum-Espresso programs was conducted to explore the electronic and optical properties of CCGS. Then, the obtained results were used to study its performance in solar cells and its photocatalytic applications. The present work is an important step towards the development of low-cost and efficient solar cells using CCGS as an absorber material.

This paper is organized as follows: Section 2 presents the details of our calculations; Section 3 provides the results of our calculations on the electronic properties; Section 4 covers the optical properties, including the dielectric function, refraction index, adsorption coefficient, and reflectivity; Sections 5 and 6 present the applications of our materials in solar cells and photocatalysis, respectively; and Section 7 provides a brief conclusion.

2. Calculations detail

The DFT (density functional theory) calculations were conducted using two software packages: WIEN2k [14], which uses the FP-LAPW method, and QUANTUM espresso [15], which uses the Plane Waves method. The Wien2K code was used with the mBJ + U potential (a combination of the Tran-Blaha modified Becke and Johnson potential and the Hubbard potential) to perform the calculations [16,17]. The QUANTUM espresso package was used to perform hybrid functional calculations. The mBJ potential, a GGA correction for the bandgap, was not sufficient to achieve results close to the experimental data, so it was combined with the Hubbard potential. These DFT methods were chosen because traditional methods (LDA and GGA) often underestimate the bandgap energy [18]. mBJ + U and hybrid functional are commonly used to correct this underestimation [19]. mBJ + U is computationally similar to traditional DFT methods, while hybrid functional is more accurate but requires more computational resources. The Hubbard potential is used for transition metal elements with strong correlation (for Cu ([Ar] $4s^1$ $3d^{10}$) and Co ([Ar] $4s^2 3d^7$)) [17]. We tested several values of U and found that 6 eV was the best value that corresponded well with the experimental data.

The Heyd-Scuseria-Ernzerhof (HSE) functional is often used for hybrid functional calculations as it can produce results close to experimental data. This approach involves combining the PBE functional with the accurate Hartree Fock exchange-correlation potential [20].

$$E_{xc}^{HSE} = \alpha E_x^{HF,SR} + (1-\alpha)E_x^{PBE,SR} + E_x^{PBE,LR} + E_c^{PBE}, \quad (1)$$

where E_c^{PBE} is the correlation energy functional of GGA-PBE, and $E_x^{PBE,SR}$, and $E_x^{PBE,LR}$ are the short-range (SR) and long-range (LR) parts of Flock the Coulombic interaction, which is range-separated to decrease the computing cost of PBE exchange. $E_x^{HF,SR}$ denotes the short-range of Hartree Fock energy, and α is the mixing parameter fixed in the original HSE functional (HSE06) to 0.25. However, this parameter can be controlled and adjusted in several cases to match the experimental results. In our situation, α is taken as 0.15.

Following convergence tests in the FP-LAPW approach the muffin-tin radii were set to be large enough to prevent overlapping. The wave functions in the interstitial region were expanded using a plane wave cut-off of $R \times K_{max} = 9$ (where K_{max} is the maximum magnitude of the k vector in the plane wave expansion). The cut-off energy for the wave function in the PW calculation was set to 80 Ry. The k-point grid in the Brillouin zone was established using the 6 × 6 × 3 grid Monkhorst-Pack method [21]. The number of K-points in the first Brillouin zone was set to 1000.

The optical properties, such as the refractive index, the absorption coefficient, and the reflectivity, are calculated from the parts of the complex dielectric function, $\varepsilon(\omega) = \varepsilon_r(\omega) + i\varepsilon_i(\omega)$, where ε_r is the real part obtained using the Kramer-Kronig transformation and ε_i is the imaginary part. The imaginary part, ε_i, can be obtained from the momentum matrix element between occupied and unoccupied states using the following equation [22]:

$$\epsilon_i(\omega) = \frac{e^2\hbar}{\pi m^2 \omega} \sum_{v,c} \int_{BZ} |\langle ck|e\nabla|vk\rangle|^2 \delta(\omega_{ck}(k) - \omega) d^3k. \quad (2)$$

3. Structural properties

The quaternary CCGS material has a tetrahedral structure characterized by the stannite phase (belonging to space group $I\bar{4}2m$ (121)) [11,23]. In the kesterite phase, the layers of Cu-Ge and Cu-Zn cations appear in sequence, while in the stannite phase the Zn-Ge layers appear alternately after the Cu-Cu (Cu2) layers [24]. The arrangement of each element in the CCGS stannite structure is illustrated in Fig. 1.

The total energy data fitted with the unit cell volume is displayed in Fig. 2. The calculated lattice parameters match the experimental measurement of $a = 5.24$ Å, $c = 10.6$ Å for the stannite structure [11]. The estimated lattice parameters using Wien2k are $a = 5.27$ Å and $c = 10.53$ Å. Meanwhile, the relaxed parameters with the BFGS method are $a = 5.23$ Å and $c = 10.54$ Å. The stability of CCGS can be analyzed by its cohesive energy, which is the energy required to break down the crystal into individual atoms. A lower cohesive energy indicates a more stable crystal structure and can be calculated using the formula [25].

$$E_C = [E_{CCGS} - 2 \times E_{Cu} - E_{Co} - E_{Ge} - 4 \times E_S] \times \frac{1}{8}, \quad (3)$$

where E_{CCGS} is the total energy of CCGS, and E_{Cu}, E_{Co}, E_{Ge}, and E_S are the

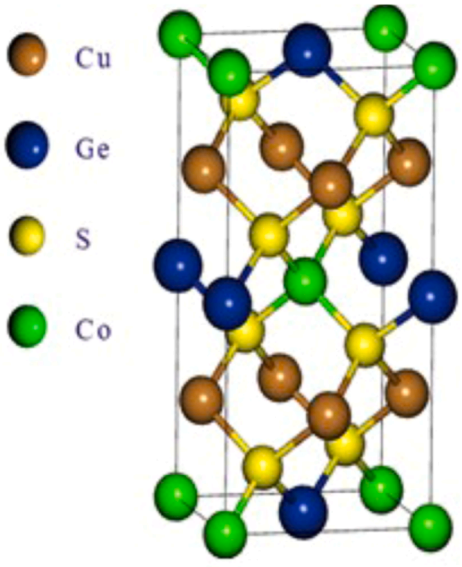


Fig. 1. Schematic representation of Cu2CoGeS4 in stannite structure.

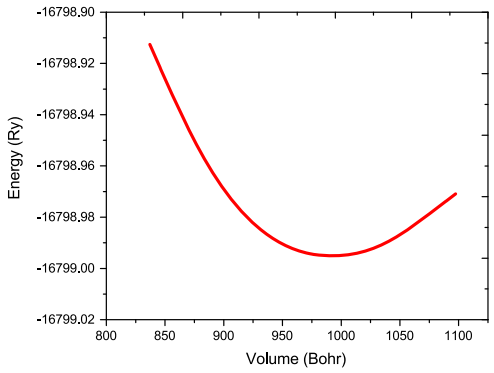


Fig. 2. The total energy as a function of volume for CCGS.

isolated atom energies in the freedom state. CCGS has computed cohesive energies of − 4.28 eV/atom. The stability of our material is shown by E_c negative sign. The obtained cohesive energies are similar to the experimentally reported Kesterite CZTS cohesion energy of 3.9 eV/atom [26].

4. Electronic properties

Before we study its characteristics, let's look at the electronic properties of Cu_2CoGeS_4. Spin polarization calculations are necessary because cobalt has a metallic property. The way that CCGS behaves electronically will differ greatly depending on the direction of the spin, whether it is up or down. Fig. 3(a) and (b) display the band structures of CCGS for both spin directions, up and down, obtained using both the mBJ + U and HSE approximations.

One can notice the influence of spin orientation on the band gap energy of CCGS. Fig. 3(a) and (b) demonstrate that mBJ + U and HSE show a direct bandgap behavior in both spin cases. For spin-up cases, the bandgap is located at the Γ valley of the first BZ. The obtained bandgap with HSE and mBJ + U approximatios are 1.73 eV and 1.78 eV respectively. The spin-down case bandgap is located at P valley with mBJ + U and Z valley with HSE. The spin-down bandgap energies are 1.8 eV and 0.78 eV with mBJ + U and HSE, respectively. We note that the band gap energies obtained for the majority spin-up of stannite CCGS are in good agreement with the experimental band gap of 1.75 eV [11].

To discuss the contributions of the different atomic orbitals, we calculate the density of states (DOS). In Fig. 3(c), we present the partial and total DOS of the main contributions forming the conduction and valence bands. As shown in the figure, for both spin configurations, the top of the valence band is formed by the *d*-orbitals of Cu. In contrast, the lower conduction band is primarily formed by the *s*-orbitals of Ge with a small contribution from the *p*-orbitals of S. The upper part of the conduction band in the spin up case is composed of the *p*-orbitals of Ge.

In contrast, the spin down case involves hybridization between the *d*-orbitals of Co and the *p*-orbitals of Ge. The band gap in CZGS decreases from 2.2 to 1.75 eV when Zn atoms are replaced with cobalt atoms.

4.1. Magnetic moment

The introduction of the Co atom in the Stannite compound can bring about magnetic behavior. As shown in Fig. 3(c), the difference in density of states between spin-up and spin-down indicates a clear magnetic property. To understand this inherent property, we have displayed in Table 3 the calculated total and partial magnetic moments that drive the magnetic character of the structure. The total magnetic moment is found to be 3 μ_B (Bohr magneton) with a significant contribution from Co's partial magnetic moment (2.3 μ_B). The magnetic contribution from other atoms is weak (0.7 μ_B). This magnetic moment confirms that the Co atom is the source of magnetization in the quaternary CCGS.

5. Optical properties

In this study, we examine the optical properties of CCGS with the aim of applying them in optoelectronic or photovoltaic fields. To do this, we determine the dielectric function, optical absorption, refractive index, extinction coefficient, and reflectivity using mBJ + U. It is important to

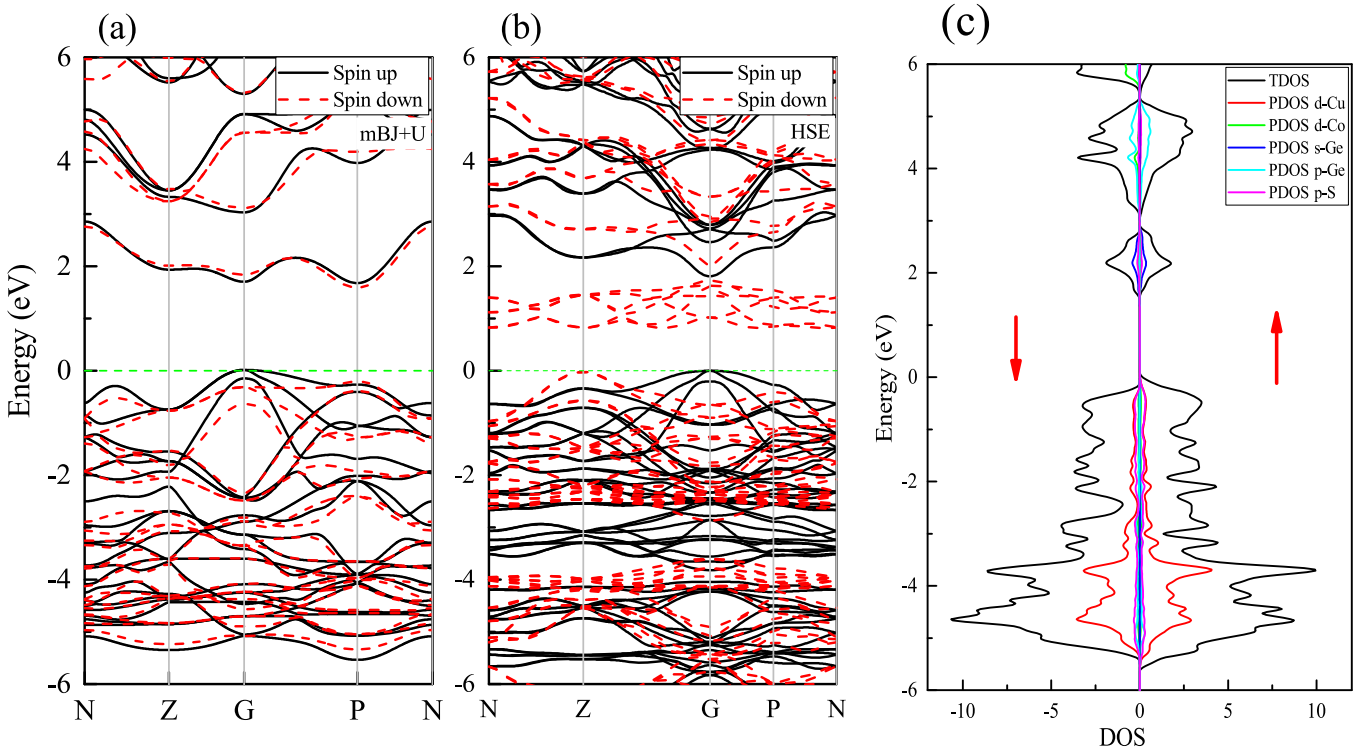


Fig. 3. The calculated band structure of CCGS with (a) mBJ + U and (b) HSE, (c) the total and partial density of state for CCGS in both spin states.

Table 1
The calculated lattice parameters, cohesion energy, band gap energy, static dielectric function, static refraction index, and the static reflectivity.

	a (Å)	c (Å)	$\|E_c\|$ (eV/atom)	E_g (eV)				ε_0	n_0	R_0 (%)
				Spin Up		Spin Down				
				HSE	mBJ + U	HSE	mBJ + U			
CCGS	5.27 (FPLAPW) 5.23 (PW)	10.53 (FPLAPW) 10.54 (PW)	4.28	1.78	1.73	0.78	1.8	6.08	2.46	17.4
EXP	5.24 [11]	10.6 [11]			1.75 [11]					

note that due to CCGS's tetragonal structure, it has two non-zero dielectric tensor components, one perpendicular (xx) to the c crystallographic axis, and the other parallel (zz) to it.

Fig. 4 shows the calculated real (ε_r) and imaginary (ε_i) components of the dielectric function for CCGS with both approximations and for two different polarization orientations. The limit value at zero frequency, which is equivalent to the static dielectric constant, is determined by averaging the longitudinal and transversal components of ε_r. The values obtained were $\varepsilon_{r-xx}(0) = 6.04$ and $\varepsilon_{r-zz}(0) = 6.12$ for the perpendicular and parallel components of the real part of ε, respectively. Furthermore, it is observed that CCGS has a negative ε_r value across the UV spectrum, making it a potential material for UV-plasmonic applications. At low energies, the plots of the parallel and perpendicular imaginary parts of the dielectric function are nearly identical, indicating that ε_i is isotropic. The spectra of ε_i show the first observable peaks near the band gap energy, which represent the first critical photon energy. These peaks correspond to a direct interband transition between the s-state of Ge and the d-state of Cu, representing the lowest conduction band and highest valence band, respectively.

The optical absorption can be predicted using measurements of the imaginary component of the dielectric function, which allows us to identify the region of the electromagnetic wave spectrum where CCGS can potentially absorb. Fig. 5 shows the in-plane and out-of-plane components of the absorption coefficient. As observed, the absorption occurs at energies greater than or equal to the CCGS gap energy and has a significant absorption coefficient, on the order of 10^4 cm^{-1}. This suggests that CCGS may be an effective absorber layer material in thin-film solar cells.

Fig. 6 shows the parallel and perpendicular components of the refractive index of stannite CCGS as a function of incoming photon energy. It is interesting to observe that n(ω) behaves similarly to ε_r (ω) and ε_i (ω). The refractive index is relatively constant in the low-frequency region, then increases with energy due to distinct electronic transitions from the valence band to the conduction band. The stannite CCGS presents a highly anisotropic refractive index behavior, exhibiting double refraction and birefringence. The birefringence, $\Delta n = n_e - n_o$, describes the difference between the extraordinary and ordinary

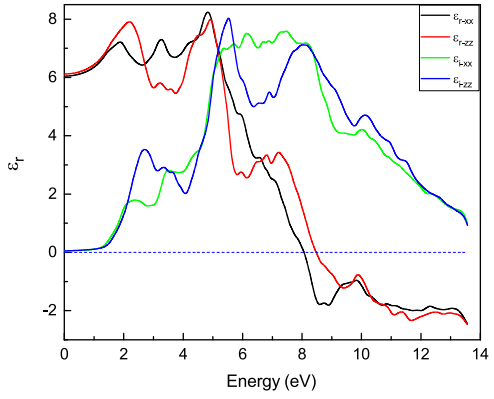


Fig. 4. The real and imaginary parts of dielectric function spectra of CCGS as functions of the incident photon energy.

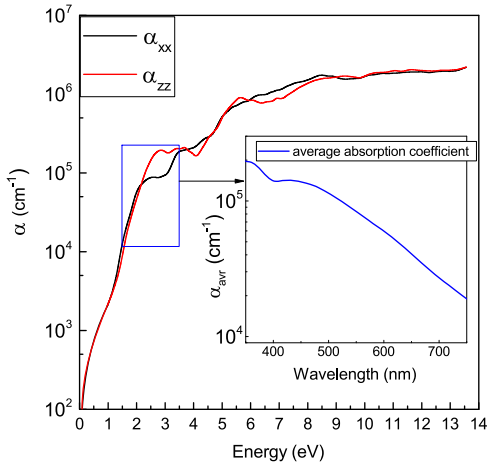


Fig. 5. The absorption coefficient spectra of CCGS as functions of the incident photon energy. The inset is the average absorption coefficient in the visible range.

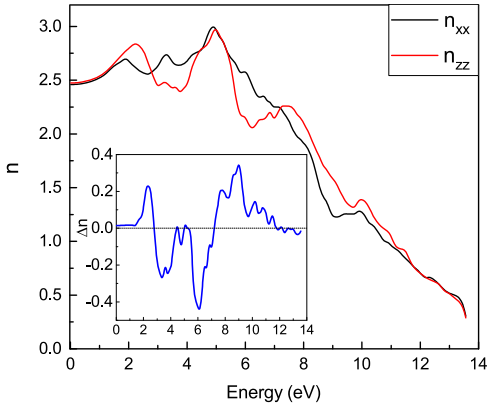


Fig. 6. The refraction index spectra of CCGS, and the inset is the birefringence as functions of the incident photon energy.

refractive indices (n_e and n_o) which represent the parallel and perpendicular refractive indices for tetragonal materials. The inset of Fig. 6 shows the calculated birefringence of CCGS, which is negative for energies less than 7.2 eV and positive for the other energy window. This behavior is consistent across all the different optical properties. The average static refractive index of CCGS is summarized in Table 1.

The computed reflectivity of stannite CCGS is displayed in Fig. 9 for both directions. The reflectivity exhibits an anisotropic behavior for energies higher than the band gap energy. The small reflectivity values at low energy suggest the potential of stannite CCGS to absorb light, making it suitable for solar cell applications. Reflectivity values generally increase with energy, but there are specific levels where there is a decrease, which is due to interband transitions. The average reflectivity at zero frequency of stannite CCGS is 17.4%.

6. Solar cell application

in order to use CCGS as an absorber layer, we perform numerical simulations of a photovoltaic solar cell using the typical CZTS device [27–29]. Fig. 7(a) shows the conventional PN junction configuration of Mo/CCGS/CdS/ZnO /ZnO:Al, where CdS acts as the n-type buffer layer, CCGS is the p-type absorber, and Mo is the back contact. The top layer of CdS is a transparent conducting oxide (TCO) consisting of intrinsic ZnO and ZnO doped with Al. The simulation is carried out using the SCAPS-1D software developed at the University of Gent in Belgium [30, 31]. By solving fundamental semiconductor equations such as the continuity equation, Poisson equation, and carrier transport equation, SCAPS can predict JV characteristics and spectral response [31–33].

SCAPS simulations require a set of device and layer input parameters, which were collected from the experimental literature or estimated using DFT [27,34–38]. Table 2 summarizes all simulation parameters. The simulation sets the work function of Mo's back contact at 5 eV, with surface recombination speeds of 10^5 cm s^{-1} and 10^7 cm s^{-1} for electrons and holes, respectively [39]. In the absorber layer, a single defect type is introduced, as in the CCGS/CdS and MoS2/CCGS heterointerfaces, with a capture cross-section of 10^{-14} cm^{-3} and a density of 10^{15} cm^{-3} [40, 41]. The electron affinity of CCGS is calculated using the formula: $\chi = 4.94 - 0.43E_g$ [42]. The simulation also includes radiative recombination, as auger recombination is significant at high carrier concentrations. The following equation is used to compute radiative recombination [43]

$$B = \frac{8\pi n_r^2}{c^2 h^3 n_i^2} \int_{E_g}^{\infty} \frac{\alpha(E) E^2 dE}{e^{\frac{E}{KbT}} - 1}, \tag{4}$$

where $\alpha(E)$ is the absorption coefficient as a function of wavelength, n_r is the material's refractive index, E_g is the band gap energy, and c is the vacuum speed of light. The conduction and valance band effective density of states is calculated using:

$$N_c = 2\left(\frac{2\pi m_e^* K_b T}{h^2}\right)^{3/2}, \tag{5}$$

$$N_v = 2\left(\frac{2\pi m_h^* K_b T}{h^2}\right)^{3/2}, \tag{6}$$

where m_e^* and m_h^* are the effective masses of electron and hole, respectively, that are determined by the parabolic fitting of the band edge using the following equation [44]:

$$m^* = \hbar\left(\frac{\partial^2 E_b}{\partial k^2}\right)^{-1}, \tag{7}$$

Table 2
Physical parameters of each layer used in the simulation of CCGS solar cell [27, 34–38]. (* Computed in this work.).

Parameters	ZnO:Al	ZnO	CdS	CCGS	MoS_2
ω	80	80	50	2000	80
E_g(eV)	3.3	3.3	22.4	1.78*	3.3
X (eV)	4.5	4.5	4.4	4.14*	4.2
ε	9	9	10	6.08*	4
n_0	2	2	2.5	2.46*	4.77
N_c (cm^{-3})	$2.2\,10^{18}$	$2.2\,10^{18}$	$2.2\,10^{18}$	$1.04\,10^{18}$*	$7.5\,10^{17}$
N_v(cm^{-3})	$1.8\,10^{19}$	$1.8\,10^{19}$	$1.8\,10^{19}$	$1.96\,10^{19}$*	$1.8\,10^{18}$
ν_e(cm /s)	10^7	10^7	10^7	10^7	10^5
ν_h (cm/s)	10^7	10^7	10^7	10^7	10^7
μ_e (cm^2/ Vs)	100	100	100	200	100
μ_h (cm^2/ Vs)	25	25	25	25	150
N_D (cm^{-3})	10^{18}	10^{18}	10^{18}	0	0
N_A (cm^{-3})	0	0	0	10^{16}	10^{15}
Absorption	Scaps file	Scaps file	Scaps file	Experimental data [38]	Data Fig. 5
$m_e^*(m_0)$	0.27	0.27	0.25	0.12*	0.53
$m_h^*(m_0)$	0.59	0.59	0.7	0.85*	0.62

Table 3
the computed magnetic moment.

	Total	Cu	Co	Ge	S
μ (μ_B)	3	0.08	2.3	0.02	0.05

where E_b is the energy of the band of interest, and k is the wave vector. The absorption coefficient data for each layer was imported from an external source; for CCGS, we use the data in Fig. 5. The other layers were collected from published experimental results [35,38]. The series and shunt resistances of CCGS solar cell were taken approximately as the practical series and shunt resistance of CZTS soar cells with 4.5 Ω cm^2 and 340 Ω cm^2, respectively [45]. The cell was illuminated with AM1.5G spectrum light from the TCO side.

The band diagram of the CCGS baseline cell is shown in Fig. 8. The energy band diagram shows the role of band alignment in the photogenerated carriers transport, carrier recombination across the heterojunction, and hence the performance of solar cells. The most crucial area of the band diagram is where the absorber (CCGS) and buffer (CdS) layers meet, where a spike-like structure is seen. Spike shape interfaces are well-known for their remarkable efficiency [46]. Indeed, it improves the collection of photogenerated electrons due to the reduction of the recombination rate at the interface, which leads to a higher V_{oc}, thus increasing the solar cell's performance.

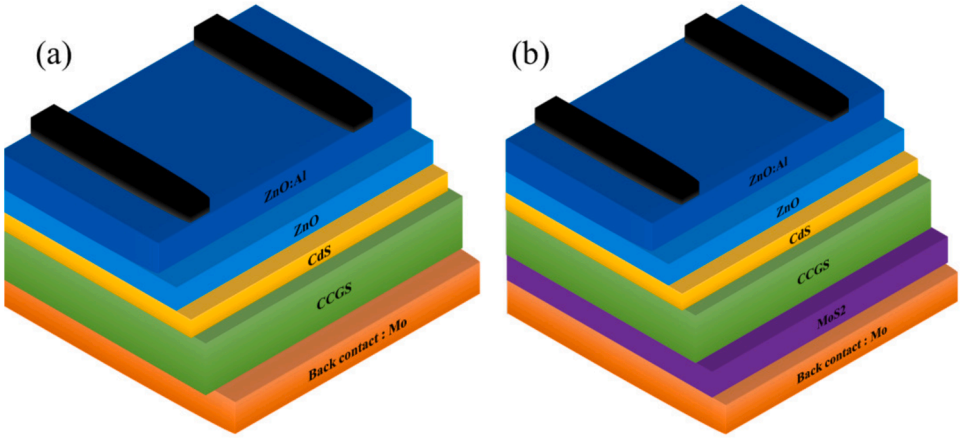


Fig. 7. The CCGS solar cell devices, a) CCGS baseline, b) CCGS baseline with MoS_2 interlayer.

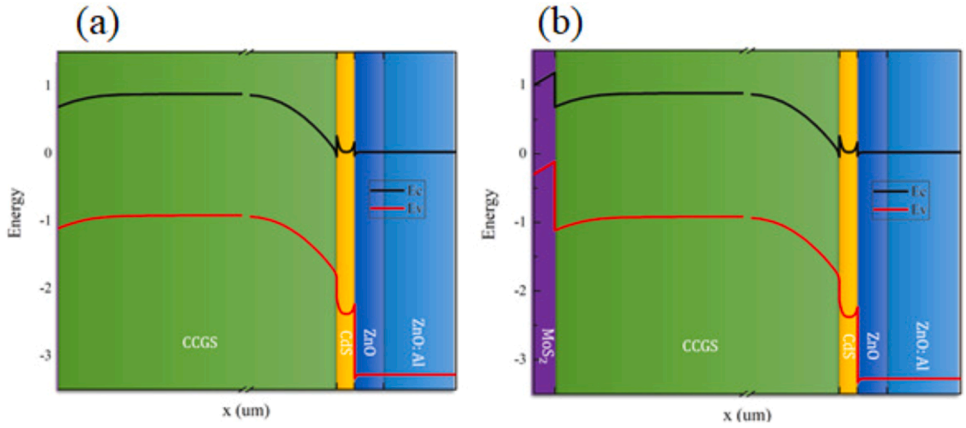


Fig. 8. Energy band diagram of CCGS solar cells (a) without MoS_2 (b) with MoS_2 interlayer.

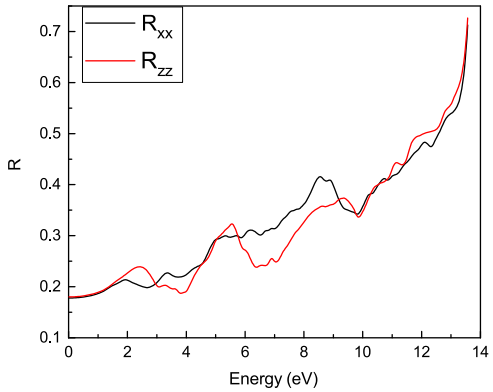


Fig. 9. The reflectivity spectra of CCGS as functions of the incident photon energy.

Fig. 10 (black plot) shows the current-voltage characteristic of the CCGS baseline, which allows us to derive the essential solar cell parameters. The efficiency of the CCGS baseline cell is 11.5%, with a fill factor of 61.67% and other parameters of 0.75 V and 24.8 mA cm^{-2} in V_{oc} and J_{sc}, respectively. It is worth mentioning that a J_{sc} value of 24.8 mA cm^{-2}, which is higher than the one expected for an absorber band gap of 1.75 eV, it is a result of extra absorption of photons due to a band tailing with energies lower than CCGS band gap as shown in Fig. 5. CCGS with a band gap of 1.75 eV should have a PCE of at least 26%, according to the Shockley-Queisser limit [47]. The 11.5%, on the other hand, falls well short of the predicted efficiency. Therefore, we add a thin layer of

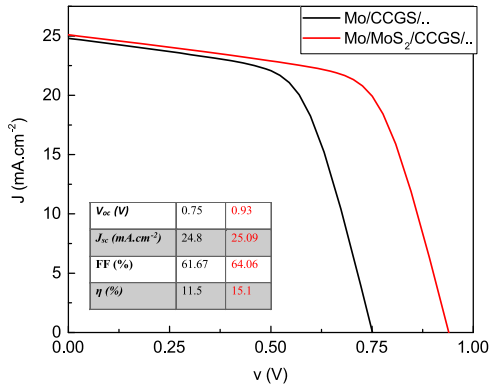


Fig. 10. J-V characteristics CCGS solar cells with and without a MoS_2 interlayer.

MoS_2 as an interlayer between CCGS and molybdenum to improve the performance of the CCGS baseline. Fig. 8(b) shows the CCGS solar cell device with MoS_2. It is been reported that the p-type MoS_2 positively influences efficiency improvement [36].

As shown in Fig. 10 (the red plot), the inclusion of the p-MoS $_2$ layer improves efficiency from 11.5% to 15.1%. Similarly, the newly obtained values for V_{oc}, J_{sc}, and FF are 930 mV, 25.09 mA cm^{-2}, and 64.06%, respectively. Although there is no significant difference in J_{sc} between the two simulated devices, the V_{oc} is greatly improved. This results in boosting the efficiency of solar cell can be attributed to rectifying the contact between MoS_2 and Mo, reducing series resistance, and increasing open circuit voltage. The MoS_2 layer is often employed in many studies to mitigate the mismatch between CZTS and Mo [37]. The MoS_2 interlayer between CCGS and molybdenum has improved the Voc. But, the device still has a low recombination resistance (Rct) leading to a low fill factor. To improve the Rct, we recommend exploring alternative buffer layers or modifying the device architecture, using passivation layers or surface treatments at the CCGS/buffer interface, and trying different doping of the material.

Having explored the potential of CCGS as an absorber layer in photovoltaic solar cells, we will examine the effect of the CCGS absorber layer thickness and doping concentration on photovoltaic response. It is widely recognized that layer thickness is a critical factor that affects device efficiency, material utilization, and cost [33]. To assess the impact of these two parameters, we varied the CCGS absorber layer thickness from 0.4 μm to 2.4 μm, concurrently with the doping concentration, which was varied from 10^{10} to 10^{18} cm^{-3}, keeping all other parameters constant for both configurations with and without MoS2 interlayer. Figs. 11 and 12 present a contour plot of J_{sc}, V_{oc}, FF, and η variations as function of both doping concentration and thickness for CCGS solar cells with and without MoS_2 interlayer. The simulation results indicate that as the absorber thickness increases, all parameters increase. This increase is primarily due to the absorption of more photons with longer wavelengths as the thickness increases.

The high absorption coefficient of 10^4 cm^{-1} results in more electron-hole pairs being formed. When the CCGS layer thickness is smaller than 500 nm (shown in blue on Figs. 11(a) and 12(a)), the device's efficiency is lower because excess carriers recombine at the back contact. A thickness of 1.9 μm is enough to absorb most incoming photons and achieve good efficiencies of over 11.5% (without MoS_2) and 16% (with MoS_2). A maximum η of 12.02% and 16.6% for CCGS-based cells without and with a MoS_2 interlayer, respectively, were observed in this work with a carrier concentration of 10^{17} cm^{-3} and a CCGS layer thickness of 2.4 μm. At lower carrier concentrations, the FF decreased slightly with increasing absorber layer thickness due to the increase in the device's series resistance. The highest values of FF were identified for all thickness ranges with a carrier concentration of around 10^{17}

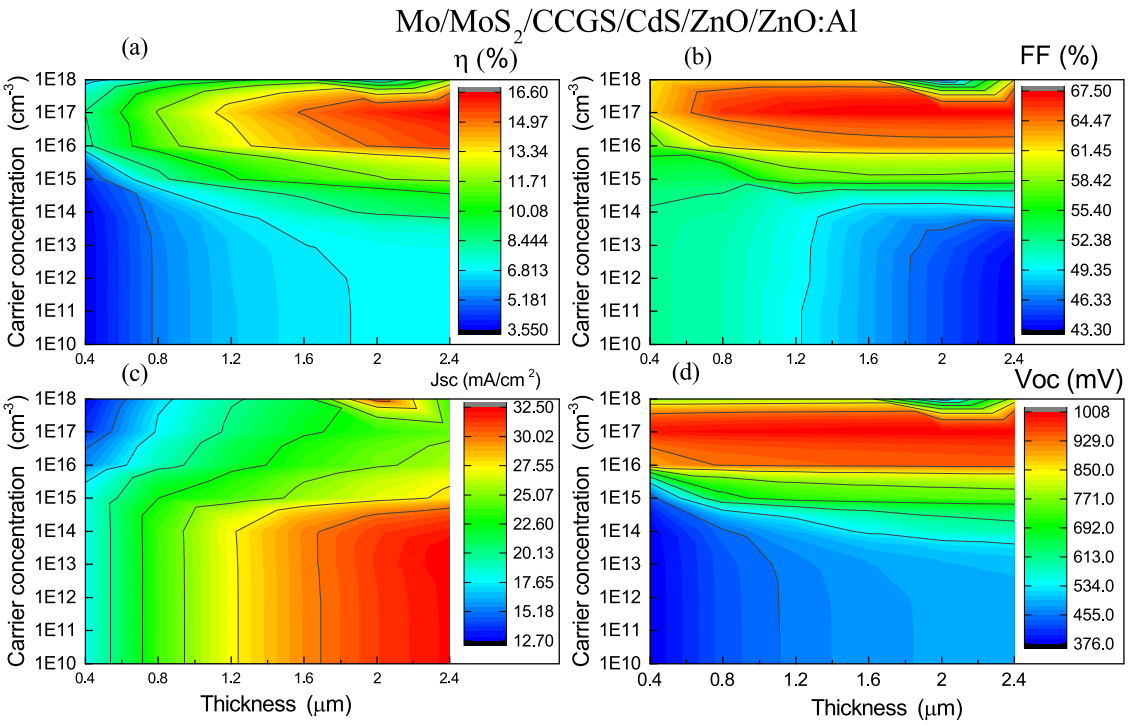


Fig. 11. influence of carrier concentration and thickness on the optoelectronic properties of CCGS solar cell with MoS2 interlayer.

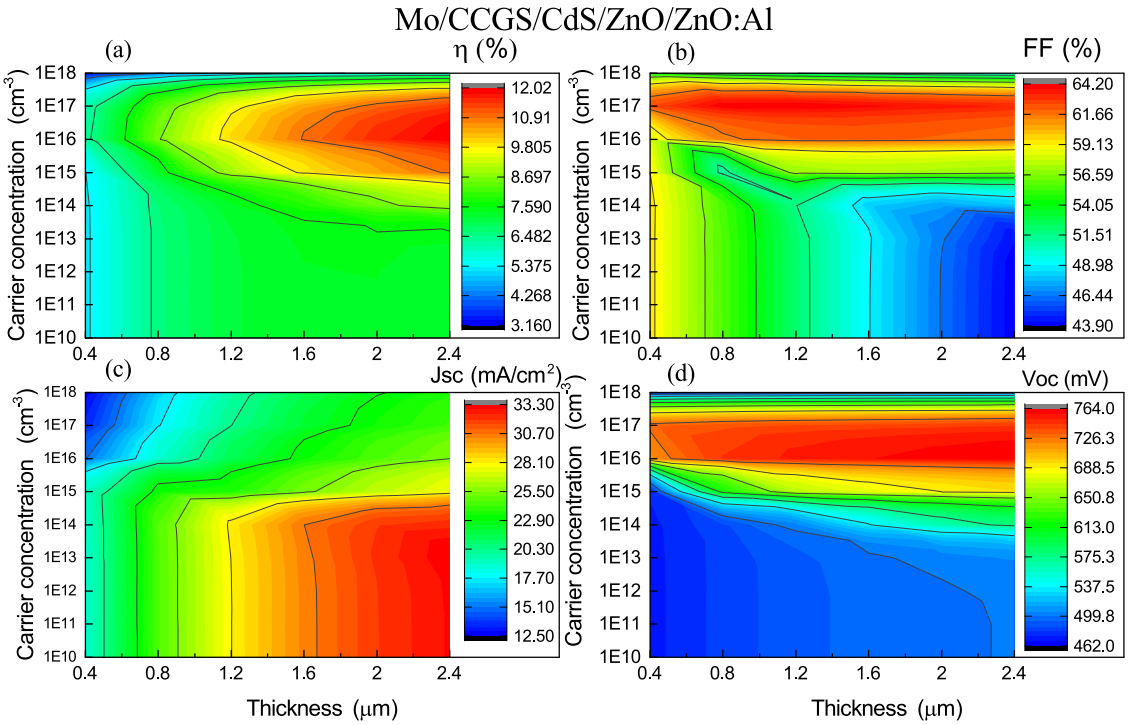


Fig. 12. The contour of the variation of solar cell performance parameters with doping concentration and thickness for CCGS cell without MoS_2 interlayer.

cm^{-3}. As shown in Figs. 11 and 12, increasing the absorber layer thickness at low carrier concentrations resulted in a systematic decrease in V_{oc}. However, a considerable increase in V_{oc} was observed when the absorber carrier concentration increased from 10^{14} to 10^{17} cm^{-3} due to a reduction in reverse saturation current. V_{oc} began to drop after the carrier concentration reached this level. As doping concentration increased, photogenerated electron lifetime decreased, limiting carrier collection at the interface and decreasing J_{sc}. The contour region with the maximum J_{sc} extended in the area with the greatest thickness and lowest carrier concentration (bottom-right). With carrier concentrations higher than 10^{15} cm^{-3}, J_{sc} collection decreased due to a narrower depletion layer. The device could yield high J_{sc} with a minimal absorber layer thickness of 1.8 μm and a carrier concentration lower than10^{15} cm^{-3}. A sharp change in all PV performance parameters was found at the start of a carrier concentration of 5.10^{17} cm^{-3}. According to

semiconductor theory, higher carrier concentration in a semiconductor deteriorates its semiconducting properties, which may cause the abrupt change in photovoltaic performance metrics. This change may be described by the "Mott transition" theory [48], which states that when a semiconductor is doped to a specific level, it loses its semiconductor properties and becomes metallic.

7. Photocatalytic water splitting

Even though commercial solar cells have attained over 20% efficiency, it is still important to store the power generated by solar panels during the day or in the summer to meet peak electricity demand at night or in the winter, due to the intermittent nature of solar energy [49]. Hydrogen (H_2) has the potential to be a sustainable power storage solution, but current H_2 production methods heavily rely on fossil fuels. On the other hand, photocatalytic water splitting provides a clean H_2 generation technology that can be combined with solar energy in various ways. The efficiency of using photovoltaic electricity to directly electrolyze water to create H_2 is mainly determined by the efficiency of the solar cells. The CCGS, with a solar cell efficiency of 16%, may hold promise as a material for photocatalytic water splitting to generate clean hydrogen (H_2).

In this section, our focus is on exploring the potential use of CCGS as an effective host material for photocatalytic water splitting and environmental applications. The CCGS compound is well-suited for photocatalytic water splitting, as its bandgap is close to the energy required to split water at a photoelectrode (which ranges from 1.6 to 2.4 eV [49]). The photocatalytic activity of CCGS can be theoretically confirmed by its bandgap and band edge potentials. However, photocatalysts with similar bandgap energies may exhibit different behaviors, and the photocatalytic behavior is influenced by the positions of the conduction band (CB) and valence band (VB) of the material on the redox potential scale. The band edge positions were calculated using the Mott–Schottky technique, based on the following relations [50]:

$$\begin{aligned} E_{vb} &= X - E_e + 0.5 \times E_g, \\ E_{cb} &= E_{vb} - Eg, \end{aligned} \tag{8}$$

where E_g is the bandgap energy, E_{vb} is the valence band potential, E_{cb} is the conduction band potential, E_e represents the energy of free electrons on the hydrogen scale (approximately 4.5 eV), and X is the electronegativity of the catalyst. The calculated values are $E_{vb} = 1.63$ and $E_{cb} = -0.11$. These findings are illustrated in Fig. 13, which shows the possible mechanism.

The calculated band edge potentials for Cu_2CoGeS_4 show a higher valence band edge potential than H_2O /O_2 (1.23 V vs. NHE), which facilitates the oxidation of water into O_2 [51]. Meanwhile, the obtained conduction band edge of CCGS is more negative than the water reduction potential in the standard hydrogen electrode (NHE) scale, which produces hydrogen at the photocatalyst interface. However, the surface electric property of the photocatalyst also influences the photocatalytic activity, as it affects the adsorption of water on the catalyst surface. This property can be modified in two ways: by adjusting the pH values of the catalyst suspension (aqueous solution), or by forming another composite to create a heterojunction. To improve the photocatalytic activity and increase the catalytic performance of CCGS, various methods have been explored, including conventional techniques like semiconductor-coupled heterojunctions [52], designing novel morphologies [53], and metal or non-metal doping (cation ion or anion ion) [54] such as Pt − CZSS and Au - CZSS heterostructure [55].

8. Conclusion

We studied Cu_2CoGeS_4 electrical and optical characteristics in its Stannite structure and came to certain conclusions. With HSE approximation, we reported a band gap energy of 1.74 eV. The reported experimental data and these results agree very well. In the visible spectrum, CCGS has an optical absorption coefficient higher than 10^4 cm^{-1}. In light of this remarkable finding, we have simulated a CCGS-based solar cell, including the influence of defects and resistances in our model. According to our results, solar cell efficiency can be as high as 15.1%. These findings suggest that CCGS Stannite is a potential absorber material. Further theoretical and experimental research is required to get a good solar cell efficiency. We also demonstrated the possibility of using CCGS for a photocatalytic water-splitting application.

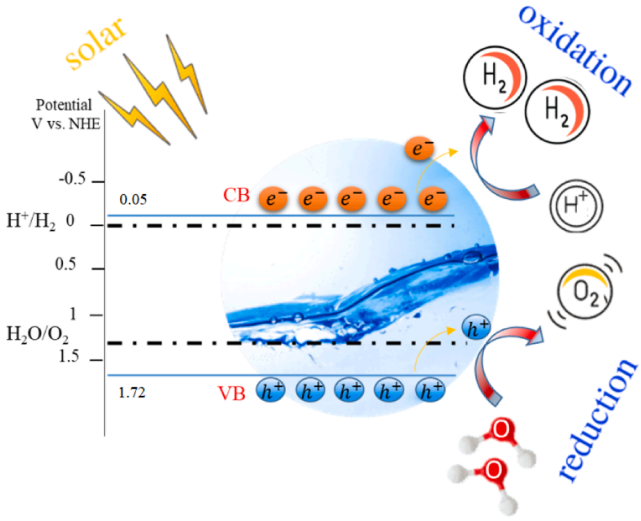


Fig. 13. Schematic diagram of the electron-hole transfer process in CCGS under light irradiation for photocatalytic water splitting.

CRediT authorship contribution statement

J. El hamdaoui: Conceptualization, Data curation, Formal analysis, Investigation, Methodology, Writing – original draft. **K. Lakaal:** Data curation, Investigation, Software. **D. Mazkad:** Formal analysis, Writing – original draft. **M. Beraich:** Formal analysis, Validation, Writing – original draft. **A. El Fatimy:** Project administration. **M. Courel:** Methodology, Validation, Writing – review & editing. **L.M. Pérez:** Funding acquisition, Resources, Supervision. **Pablo Díaz:** Software, Validation. **D. Laroze:** Funding acquisition, Resources, Visualization. **E. Feddi:** Conceptualization, Funding acquisition, Investigation, Project administration, Resources, Supervision, Visualization, Writing – review & editing.

Declaration of Competing Interest

Authors declare that they have no conflict of interest.

Data availability

No data was used for the research described in the article.

Acknowledgments

The authors thank the technical and computational support of M. J. Suazo (UTA, Chile). LMP acknowledges financial support from ANID through Convocatoria Nacional Subvención a Instalación en la Academia Convocatoria Año 2021, Grant SA77210040. DL acknowledges partial financial support from the Centers of Excellence with BASAL/ANID financing, AFB220001, CEDENNA. This research was supported through computational resources of HPC-MARWAN provided by the National Center for Scientific and Technical Research (CNRST).

References

[1] C. Coughlan, M. Ibanez, O. Dobrozhan, A. Singh, A. Cabot, K.M. Ryan, Compound copper chalcogenide nanocrystals, Chem. Rev. 117 (9) (2017) 5865–6109.

[2] R.A. Almotiri, M.M. Alkhamisi, A.R. Wassel, A.M. El-Mahalawy, Optical dispersion and photovoltaic performance of safranin thin films solar cells in hybrid organic-inorganic isotype heterojunction configuration, Mater. Res. Bull. 151 (2022) 111824.

[3] S. Ji, C. Ye, Cu_2ZnSnS_4 as a new solar cell material: the history and the future, Rev. Adv. Sci. Eng. 1 (1) (2012) 42–58.

[4] M.S. Kumar, S.P. Madhusudanan, S.K. Batabyal, Substitution of Zn in earth-abundant $Cu_2ZnSn(S,Se)_4$ based thin film solar cells—A status review, Sol. Energy Mater. Sol. Cells 185 (2018) 287–299, https://doi.org/10.1016/j.solmat.2018.05.003.

[5] J. Huang, Y. Yuan, Y. Shao, Y. Yan, Understanding the physical properties of hybrid perovskites for photovoltaic applications, Nat. Rev. Mater. 2 (7) (2017) 1–19.

[6] M. Quintero, E. Moreno, S. Alvarez, J. Marquina, C. Rincón, E. Quintero, P. Grima, J.-A. Heano, M.A. Macías, Lattice parameter values and phase transitions for the Cu_2-II-IV-S_4 (Se_4)(II = Mn, Fe, Co; IV = Si, Ge, Sn) magnetic semiconductor compounds, Rev. Latinoam. Metal. Mater. 34 (1) (2014) 28–38.

[7] M. Beraich, H. Shaili, E. Benhsina, Z. Hafidi, M. Taibi, F. Bentiss, A. Guenbour, A. Bellaouchou, A. Mzerd, A. Zarrouk, et al., Experimental and theoretical study of new kesterite Cu_2NiGeS_4 thin film synthesized via spray ultrasonic technic, Appl. Surf. Sci. 527 (2020) 146800.

[8] P. Kush, S. Deka, Multifunctional copper-based quaternary chalcogenide semiconductors toward state-of-the-art energy applications, ChemNanoMat 5 (4) (2019) 373–402.

[9] I. Mustafa, M.M. Koç, Infrared sensing properties of quaternary Cu_2CoSnS_4 photodetectors, J. Mater. Electron. Devices 1 (1) (2020) 19–24.

[10] M. Krishnaiah, Y.J. Jeong, R.K. Mishra, M.J. Kim, J. Song, S.H. Jin, Temperature-time profile effects on evolution of physical and electronic properties in visible light Cu_2CoSnS_4 photodetectors, Mater. Sci. Semicond. Process. 121 (2021) 105443.

[11] M. Beraich, H. Shaili, E. Benhsina, Z. Hafidi, M. Taibi, F. Bentiss, A. Guenbour, A. Bellaouchou, S. Mansouri, A. Mzerd, et al., Structural, electronic and optical properties of a tetragonal-stannite Cu_2CoGeS_4 thin film synthesized by a low-cost spray method: experimental and theoretical study, Ceram. Int. 46 (14) (2020) 23127–23133.

[12] L.D. Gulay, O.P. Nazarchuk, I.D. Olekseyuk, Crystal structures of the compounds $Cu_2CoSi(Ge, Sn)S_4$ and $C_2CoGe(Sn)Se_4$, J. Alloys Compd. 377 (2004).

[13] T. Bernert, A. Pfitzner, Characterization of mixed crystals in the system $Cu_2Mn_xCo_{1-x}GeS_4$ and investigations of the tetrahedra volumes, Z. Anorg. Allg. Chem. 632 (7) (2006) 1213–1218.

[14] K. Schwarz, P. Blaha, G.K.H. Madsen, Electronic structure calculations of solids using the WIEN2k package for material sciences, Comput. Phys. Commun. 147 (1-2) (2002) 71–76.

[15] P. Giannozzi, S. Baroni, N. Bonini, M. Calandra, R. Car, C. Cavazzoni, D. Ceresoli, G.L. Chiarotti, M. Cococcioni, I. Dabo, et al., Quantum espresso: a modular and open-source software project for quantum simulations of materials, J. Phys. 21 (39) (2009) 395502.

[16] F. Tran, P. Blaha, Accurate band gaps of semiconductors and insulators with a semilocal exchange-correlation potential, Phys. Rev. Lett. 102 (22) (2009) 226401.

[17] N.E. Kirchner-Hall, W. Zhao, Y. Xiong, I. Timrov, I. Dabo, Extensive benchmarking of DFT+U calculations for predicting band gaps, Appl. Sci. 11 (5) (2021) 2395.

[18] J.P. Perdew, K. Burke, Y. Wang, Erratum: generalized gradient approximation for the exchange-correlation hole of a many-electron system, Phys. Rev. B 57 (23) (1998) 14999.

[19] A. Shokri, A. Yazdani, K. Rahimi, Tunable electronic and optical properties of g-ZnO/α-PtO_2 van der Waals heterostructure: a density functional theory study, Mater. Chem. Phys. 255 (2020) 123617.

[20] J. Heyd, G.E. Scuseria, M. Ernzerhof, Hybrid functionals based on a screened coulomb potential, J. Chem. Phys. 118 (18) (2003) 8207–8215.

[21] H.J. Monkhorst, J.D. Pack, Special points for brillouin-zone integrations, Phys. Rev. B 13 (12) (1976) 5188.

[22] J. El Hamdaoui, M. El-Yadri, M. Farkous, M. Kria, M. Courel, M. Ojeda, L.M. Pérez, A. Tiutiunnyk, D. Laroze, E.M. Feddi, Strain effects on the electronic and optical properties of kesterite Cu_2ZnGeX_4 (X = S, Se): first-principles study, Nanomaterials 11 (10) (2021) 2692.

[23] C. Rincón, M. Quintero, C. Power, E. Moreno, E. Quintero, J.A. Henao, M. A. Macías, M. Morocoima, Raman spectra of $Cu_2BIICIVX_4$ VI magnetic quaternary semiconductor compounds with tetragonal stannite type structure, J. Appl. Phys. 117 (20) (2015) 205701.

[24] S.R. Hall, J.T. Szymanski, J.M. Stewart, Kesterite, Cu_2(Zn, Fe)SnS_4, and stannite, Cu_2(Fe, Zn)SnS_4, structurally similar but distinct minerals, Can. Mineral. 16 (2) (1978) 131–137.

[25] X.F. Wang, W. Li, G.P. Fang, C.W. Wu, J.G. Lin, First-principles calculations on the electronic structure and cohesive properties of titanium stannides, Intermetallics 17 (9) (2009) 768–773.

[26] S.R. Rondiya, Y. Jadhav, N.Y. Dzade, R. Ahammed, T. Goswami, A. De Sarkar, S. Jadkar, S. Haram, H.N. Ghosh, Experimental and theoretical study into interface structure and band alignment of the $Cu_2Zn_{1-x}Cd_xSnS_4$ heterointerface for photovoltaic applications, ACS Appl. Energy Mater. 3 (6) (2020) 5153–5162.

[27] S. Kukreti, G.K. Gupta, A. Dixit, Theoretical DFT studies of Cu_2HgSnS_4 absorber material and Al:Zno/ZnO/CdS/Cu_2HgSnS_4/back contact heterojunction solar cell, Sol. Energy 225 (2021) 802–813.

[28] P. Jackson, R. Wuerz, D. Hariskos, E. Lotter, W. Witte, M. Powalla, Effects of heavy alkali elements in Cu(In, Ga)Se_2 solar cells with efficiencies up to 22.6%, Phys. Status Solidi (RRL)–Rapid Res. Lett. 10 (8) (2016) 583–586.

[29] J. El Hamdaoui, M. El-Yadri, K. Lakaal, M. Kria, M. Courel, M. Ojeda, L.M. Pérez, D. Laroze, E. Feddi, Ab initio study on electronic and optical properties of Cu_2NiGeS_4 for photovoltaic applications, Sol. Energy 237 (2022) 333–339.

[30] M. Burgelman, K. Decock, S. Khelifi, A. Abass, Advanced electrical simulation of thin film solar cells, Thin Solid Films 535 (2013) 296–301.

[31] M. Burgelman, P. Nollet, S. Degrave, Modelling polycrystalline semiconductor solar cells, Thin Solid Films 361 (2000) 527–532.

[32] A. Niemegeers, M. Burgelman, Effects of the Au/CdTe back contact on IV and CV characteristics of Au/CdTe/CdS/TCO solar cells, J. Appl. Phys. 81 (6) (1997) 2881–2886.

[33] M. Minbashi, A. Ghobadi, M.H. Ehsani, H.R. Dizaji, N. Memarian, Simulation of high efficiency SnS-based solar cells with SCAPS, Sol. Energy 176 (2018) 520–525.

[34] M. Courel, J.A. Andrade-Arvizu, O. Vigil-Galán, The role of buffer/kesterite interface recombination and minority carrier lifetime on kesterite thin film solar cells, Mater. Res. Express 3 (9) (2016) 095501.

[35] H. Fujiwara, R. Collins, Spectroscopic Ellipsometry for Photovoltaics Volume 1: Fundamental Principles and Solar Cell Characterization: Volume 1: Fundamental Principles and Solar Cell Characterization, 2018. 10.1007/978-3-319-75377-5.

[36] H. Luo, Y. Zhang, H. Li, Effect of MoS_2 interlayer on performances of copper-barium-tin-sulfur thin film solar cells via theoretical simulation, Sol. Energy 223 (2021) 384–397.

[37] A.D. Adewoyin, M.A. Olopade, M. Chendo, Enhancement of the conversion efficiency of Cu_2ZnSnS_4 thin film solar cell through the optimization of some device parameters, Optik 133 (2017) 122–131.

[38] A.R. Beal, H.P. Hughes, Kramers–Kronig analysis of the reflectivity spectra of 2H-MoS_2, 2H-$MoSe_2$ and 2H-$MoTe_2$, J. Phys. C 12 (5) (1979) 881.

[39] L. Et-taya, T. Ouslimane, A. Benami, Numerical analysis of earth-abundant $Cu_2ZnSn(S_xSe_{1-x})_4$ solar cells based on spectroscopic ellipsometry results by using SCAPS-1d, Sol. Energy 201 (2020) 827–835.

[40] J. Li, Z.-K. Yuan, S. Chen, X.-G. Gong, S.-H. Wei, Effective and noneffective recombination center defects in Cu_2ZnSnS_4: significant difference in carrier capture cross sections, Chem. Mater. 31 (3) (2019) 826–833.

[41] S. Chen, J.-H. Yang, X.-G. Gong, A. Walsh, S.-H. Wei, Intrinsic point defects and complexes in the quaternary kesterite semiconductor Cu_2ZnSnS_4, Phys. Rev. B 81 (24) (2010) 245204.

[42] S. Adachi, Earth-Abundant Materials for Solar Cells: Cu_2-II-IV-VI_4 Semiconductors, John Wiley & Sons, 2015.

[43] T. Jiménez, D. Seuret-Jiménez, O. Vigil-Galán, M.A. Basurto-Pensado, M. Courel, $Sb_2(S_{1-x}Se_x)_3$ solar cells: the impact of radiative and non-radiative loss mechanisms, J. Phys. D 51 (43) (2018) 435501.

[44] M. Farkous, M. El-Yadri, H. Erguig, L.M. Pérez, D. Laroze, C.V. Nguyen, N.T. T. Binh, N.N. Hieu, H.V. Phuc, M. Sadoqi, et al., Anisotropy of effective masses induced by strain in Janus MoSSe and WSSe monolayers, Physica E 134 (2021) 114826.

[45] S. Karthick, S. Velumani, J. Bouclé, Experimental and SCAPS simulated formamidinium perovskite solar cells: a comparison of device performance, Sol. Energy 205 (2020) 349–357.

[46] A. Haddout, A. Raidou, M. Fahoume, A review on the numerical modeling of CdS/CZTS-based solar cells, Appl. Phys. A 125 (2) (2019) 1–16.

[47] W. Shockley, H.J. Queisser, Detailed balance limit of efficiency of $p-n$ junction solar cells, J. Appl. Phys. 32 (3) (1961) 510–519.

[48] N.F. MOTT, Metal-insulator transition, Rev. Mod. Phys. 40 (1968) 677–683, https://doi.org/10.1103/RevModPhys.40.677.

[49] A.S. Nazligul, M. Wang, K.L. Choy, Recent development in earth-abundant kesterite materials and their applications, Sustainability 12 (12) (2020) 5138.

[50] B. Radha, R. Rathi, K.C. Lalithambika, A. Thayumanavan, K. Ravichandran, S. Sriram, Effect of fe doping on the photocatalytic activity of ZnO nanoparticles: experimental and theoretical investigations, J. Mater. Sci. 29 (16) (2018) 13474–13482.

[51] D.-P. Bui, M.-T. Pham, H.-H. Tran, T.-D. Nguyen, T.M. Cao, V.V. Pham, Revisiting the key optical and electrical characteristics in reporting the photocatalysis of semiconductors, ACS Omega 6 (41) (2021) 27379–27386.

[52] M. Zubair, A. Razzaq, C.A. Grimes, S.-I. In, Cu_2ZnSnS_4 (CZTS)-ZnO: a noble metal-free hybrid z-scheme photocatalyst for enhanced solar-spectrum photocatalytic conversion of CO_2 to CH_4, J. CO2 Util. 20 (2017) 301–311.

[53] L. Wang, W. Wang, S. Sun, A simple template-free synthesis of ultrathin Cu_2ZnSnS_4 nanosheets for highly stable photocatalytic H_2 evolution, J. Mater. Chem. 22 (14) (2012) 6553–6555.

[54] F. Ozel, E. Aslan, B. Istanbullu, O. Akay, I.H. Patir, Photocatalytic hydrogen evolution based on Cu_2ZnSnS_4, Cu_2NiSnS_4 and Cu_2CoSnS_4 nanocrystals, Appl. Catal. B 198 (2016) 67–73.

[55] X. Yu, A. Shavel, X. An, Z. Luo, M. Ibáñez, A. Cabot, Cu_2ZnSnS_4-pt and Cu_2ZnSnS_4-Au heterostructured nanoparticles for photocatalytic water splitting and pollutant degradation, J. Am. Chem. Soc. 136 (26) (2014) 9236–9239.